Genetic Algorithm-based control of the wake of a bluff body

Genetic Algorithm-based control of the wake of a bluff body

Journal of Physics: Conference Series **2293** (2022) 012016 doi:10.1088/1742-6596/2293/1/012016

Genetic Algorithm-based control of the wake of a bluff body

Enrico Amico, Domenico Di Bari, Gioacchino Cafiero, Gaetano Iuso

Corso Duca degli Abruzzi 24, Dipartimento di Ingegneria Meccanica e Aerospaziale, Politecnico di Torino, 10129, Torino

E-mail: enrico.amico@studenti.polito.it

E-mail: gioacchino.cafiero@polito.it

Abstract. This work reports on the application of a Genetic Algorithm (GA)-based approach to control the wake of a bluff body. The control is achieved through the actuation of four air jets placed along the edges of the model's base. The dependence of the population size on the convergence of the genetic code was assessed, evidencing an increase of the number of elements in the population needed to learning more complex tasks. In this case, a sum of two sine waves is considered, where frequency and amplitude of each of the two sine waves are optimised.

It is demonstrated that the GA converges to a control law yielding values of the drag reduction up to 11.2% with respect to the natural case. The cost function has been defined as to minimise the drag coefficient, without accounting for the energy spent in the actuation.

The proper orthogonal decomposition (POD) applied to the fluctuating pressure signals highlights the most relevant features of the wake. The results show that in the natural case nearly 80% of the modal energy is associated with the first mode. Conversely, the forced case features a more evenly distributed energy content across the POD modes.

The analysis of the first two modes reveals that for both cases the wake is governed by the shedding phenomenon. Furthermore, the analysis reveals that regardless of the actuation conditions, the top-down shedding represents the most significant phenomenon for the wake dynamics.

1. Introduction

The effect of aerodynamic drag in the automotive sector covers a key role in the fuel consumption, with immediate implications on to the emission of hazardous gas. At typical speeds on motorways, 130 km/h, the aerodynamic drag can account for 80% of the total drag, while at 80 km/h it represents 50% [1]. According to a study conducted in the US and UK, fuel consumption impacts for $20 - 30\%$ on operating costs [2]. Reducing drag means reducing operating costs. These considerations are also of particular interest in the light of the continuous effort by the World community aimed at minimizing the pollution associated with the transport sector.

Despite these data show the need to minimize the aerodynamic drag, heavy duty vehicles' design is generally driven by the need to accommodate goods, hence to maximize their storage. The shape is then quite often poor from the aerodynamic standpoint, being representative of a bluff body geometry.

The aerodynamic drag of a bluff body is mainly associated with the pressure imbalance between the front and the rear of the vehicle. The large separation occurring at the base,

associated with the separating shear layers from the vehicle's edges, leads to a massive low pressure region. Controlling the near wake of these vehicles can lead to significant improvements in their aerodynamic performance.

The shape of road vehicles is such that it generates a complex wake dynamics. Numerous investigations have focused on the near-wake dynamics, which is also affected by the geometric parameters of the model [3]. The time-averaged flow field is characterized by two large recirculating regions, respectively associated with the separation of the shear layer from the top and bottom edges of the model's base [4, 5]. Despite from the time-averaged perspective the flow field can be still considered as symmetric with respect to the vertical plane, the turbulent wake undergoes a series of stochastic switches between non-symmetric states [3, 6, 7]. Similar results have also been found in the laminar regime, as evidenced by the numerical simulations reported by [8].

More recently, Haffner et al. [9] concluded that symmetry breaking can occur when the Reynolds number is large enough as to create a flow in the underbody such that the upper and lower shear layers interact to create recirculation in the base.

Taming the dynamics of the wake is therefore a key enabler towards obtaining significant drag reductions. In this sense, flow control techniques can cover a key-role. They can be generally divided into two groups: passive and active. The former do not require any power supply to function, but their implementation can be cumbersome, especially due to restrictions related to certification issues and/or due to the presence of appendages that can increase the length of the vehicle. Examples, not only limited to drag reduction, can be found in [10, 11, 12, 13, 14, 15, 16, 17, 18]. The main limitation of the passive devices is associated with the fact that they are designed for one working configuration. Hence, their performance decreases dramatically when working off-design.

Active techniques, which require a dedicated power supply to function, can be more appealing from the implementation point of view, since they are not geometrically invasive. The values of drag reduction that can be attained are generally much higher, with the drawback of lower reliability due to the presence of moving parts. Some examples are reported in [19, 20, 21, 22, 23, 24]. Other examples are related to the efficient implementation of the spanwise wall oscillation, as reported in the recent DNS investigation by Marusic et al. [25].

The vast majority of the active flow control applications to the drag reduction of bluff bodies is based on the implementation of continuous or pulsed jets at the rear base of the model. Examples are the works by [4, 26, 27], where also the combination of active (pulsed/continuous jets) and passive (Coanda effect) control is exploited. Haffner et al. [9] evidenced that all the methodologies used to control the asymmetry mechanism are based on the prevention of feedback between the opposing shear layers, which is at the origin of bi-modality.

Despite the excellent results that were obtained in previous investigations, the effectiveness of these methodologies was often limited by the selection process of the control parameters. Given the complexity of the flow, they were defined on the basis of simplistic models or through trial and error. The advancement of data-driven techniques, as well as the available computational power, makes these approaches viable and appealing for applications to fluid mechanics, both in the framework of flow predictions [28, 29] and for the closed-loop control [24, 30, 31, 32, 33].

Minelli et al. [24] implemented a genetic approach to study the sensitivity of the wake to the location of the flow control. They showed that controlling the boundary layer at the front pillar the performance of the control strategy improves significantly. The drawback is the less straightforward implementation of the flow control system in that portion of the vehicle.

Cerutti et al. [4] carried out an experimental investigation to determine the effectiveness of continuous blowing in the near wake of a square-back road vehicle. The four air jets were located along the edges of the model's base. The authors evidenced that continuous forcing can lead to drag reduction as large as $\sim 12.7\%$. They also showed that the optimal forcing can be tailored

to minimize the energy consumption, leading to lower values of drag reduction $\sim 7\%$.

The present investigation builds on the results obtained in [4] and proposes a new genetic algorithm (GA) based framework to define the jets' actuation.

This paper is structured as follows: in section 2 the experimental setup is described, along with the implementation of the active flow control system. In section 3 the genetic algorithm and its implementation are briefly discussed. In section 4 the main results are reported and discussed. Finally the conclusions and future outlook are reported in section 5.

2. Experimental Setup

The experiments are carried out in the open-circuit wind tunnel at Politecnico di Torino. The flow is accelerated by two fans located upstream of a stagnation chamber. The air flow is then conveyed to the test section through a convergent duct.

The test section has a rectangular cross-section (0.9m high and 1.2m wide) and a length of 6.5m; it is characterized by a small divergence angle of $\sim 1\%$ to account for the growth of the boundary layer on the wind tunnel walls.

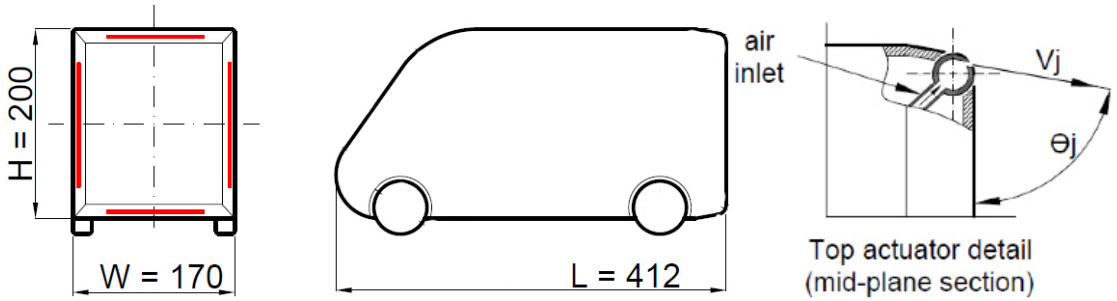

Figure 1: a) Schematic representation of the model used for the wind tunnel experiments with indication of the dimensions in mm. The continuous red line represent the injection slots of the active flow control system. b) Detail of the cylindrical actuator.

The test speed is regulated by evaluating the pressure ratio between the inlet and the outlet of the convergent, which was carefully calibrated against the readings of a Pitot tube located in the test section.

The model used ([4],[5], [34]) is representative of a $1:10$ scaled model of a square-back road vehicle typically employed as heavy duty vehicle. It is characterised by a section with a maximum height $H = 0.2m$ and a width $W = 0.17m$. A back slant angle of $10°$ (as shown in figure 1) allows to emphasize the effect of the active control system as shown in [27], exploiting the Coanda effect.

The model is held in position with a vertical strut connected to its top surface. The resulting gap between the underbody and the wind tunnel floor is equal to $g = 20$mm ($g/W = 0.1$). The strut is embedded in an aerodynamically shaped wing profile (NACA 0020, with maximum thickness $t/c = 0.2$ and $c/W = 0.07$). The strut rigidly connects the model to a load cell located outside the test section to perform the drag measurements. The fairing is also used to carry the pneumatic lines that feed the air jets, the connection cables to the pressure scanner that is located within the model and the acquisition signals. The frontal area of the model is equal to 3.1% of the cross section of the wind tunnel; this value increases to 4.5% considering also the strut fairing.

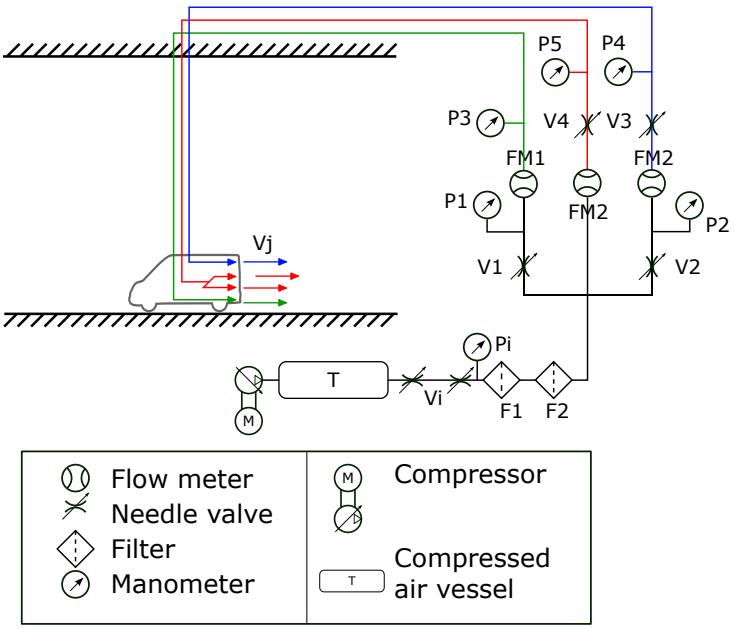

Figure 2: Schematic representation of the pneumatic system feeding the air jets.

The positioning of the model in the wind tunnel is carefully defined to account for several issues that are typical of automotive testing. The absence of the moving floor inevitably modifies the structure of the underbody flow. While this can be a significant issue when performing downforce measurements, its effect on the measurement of the drag coefficient is much less relevant. A large number of investigations are indeed performed with a stationary floor and steady wheels [3, 6, 16]. More recently, Wang et al. [34] have carried out a comparison of wind tunnel data obtained on the model employed for the present investigation with numerical simulations to quantify this effect. The authors confirmed that the main effect is on the lift coefficient and that the effect on the drag coefficient is to within 5%.

In addition to this, to minimize the boundary layer growth developing on the wind tunnel floor a suction slit is located at about two model's length upstream of the model's nose. The resulting boundary layer characteristics, as measured by dedicated hot wire anemometry experiments, are such that $\delta^*/g = 0.07$, with δ^* being the displacement thickness of the boundary layer. This value is in good agreement with other investigations performed with a stationary floor [35].

2.1. Active Flow Control system

The flow control system is constituted of four air jets located along the edges of the model's base, as schematically represented in figure 1. The individual actuator is made up of a cylinder with a rectangular slot of 1 mm along its length. The geometry is selected as to allow the orientation of the air jet along different injection angles. In the present case, a fixed injection angle of $\theta_j = 65°$ (see figure 1b) is considered. The slots have a length of $104mm$ in the case of the top and bottom slots, and $132mm$ in the case of lateral slots. Hot wire anemometry measurements were performed to characterize the velocity profile at the exit section of the slot. The velocity profile is uniform for at least 95% of the length of the slot.

A schematic representation of the the air supply that feeds the jets is reported in figure 2. A pneumatic line with a maximum operating pressure of 10 bar feeds the system. The air flow rate that feeds each of the slots is measured using three independent flow meters (FM). The three FM are connected to the top, bottom and the two lateral jets. This necessarily results

into a symmetric actuation with respect to the symmetry plane of the vehicle (XY plane).

The flow rate can be then modulated according to different control laws, such as continuous, square wave, sinusoidal wave, sawtooth, through the solenoid valves (V). In the present case, a combination of two sine waves is considered for the control law. The GA algorithm will optimize the values of the amplitude and the frequency of the sine waves. The time needed for the GA to converge to a solution is an increasing function of the population size. Since increasingly larger values of the population are required for more complex tasks, the case of same actuation law for each of the solenoid valves is investigated in this work.

2.2. Measurement system

The model is instrumented to acquire static pressure sensors using multi-input pressure transducers and microphone capsules for measuring pressure fluctuations. In particular, the static pressure signals are acquired by means of a Scanivalve connected to a Smart Zoc 100. The system allows to acquire 64 simultaneous pressure signals at a frequency $f = 100Hz$. The transducer has a full scale of $2.5kPa$ and an accuracy of $0.15\%FS$. The 64 channels are connected by pneumatic connections (tubes with an internal diameter equal to $\Phi = 1mm$) to the pressure taps. The taps are distributed as follows: 31 populate the model's base and 33 are distributed across the front, top and lateral surfaces of the model.

Furthermore, 16 microphone capsules with an external diameter of 9.8 mm and a sensing element with a diameter of 1 mm are used. The 16 capsules are distributed as follows: 12 microphones are placed across the base and the remaining 4 are placed on the four side faces at a distance of $10mm$ from the edges. The microphones have a flat response in the frequency range $0.005 - 13kHz$ and a sensitivity of $-60dB$. As shown in [4] all the sensors have been calibrated using a *Bruel & Kjaer* probe, as reported in [36]. For both measurement and calibration, a *pinhole* configuration was used and the electrical signal was filtered to eliminate spurious contributions [36].

The drag measurement is performed using a one-axis load cell *Dacell UU-K002* with a full scale $F.S. = 2\ Kg_f$ and an accuracy of $0.2\%F.S.$. The load cell signal is sampled using a NI-cDAQ chassis with a dedicated A/D converter module *A/D NI-9215* . The electrical signal of the load cell is converted into drag through a dedicated calibration mapping.

3. Genetic algorithm optimization

In this work, the genetic algorithm was implemented using the library included in Matlab, which is based on the work reported in [37] and [38]. The optimization problem is introduced through the fitness (or cost) function (FF) defined as the difference between the drag coefficient under natural conditions $\overline{Cd}_0$ and that under forcing conditions $\overline{Cd}$

$$FF = \overline{Cd}_0 - \overline{Cd} \tag{1}$$

where the overline indicates the ensemble average operation over a given acquisition time.

The value of the two coefficients is measured at each evaluation of the cost function. The acquisition of the signal lasts $t_a = 30s$ keeping constant the value of the control parameters: amplitude and frequency of the actuators.

A schematic representation of the working principle of the GA algorithm is shown in figure 3. Initially, $\overline{Cd}_0$ is measured in order to establish the reference value. For the first generation, random parameters are defined for the control law.

The value of $\overline{Cd}$ is then measured under the first set of actuation laws, so that the cost function can be evaluated. The same procedure is repeated for each element of the generation, i.e. a number of times equal to the population size. At the end of this process the selected GA operations (elitism, cross-over and mutation) are performed to determine the new set of control laws. The generation size defines the number of times that the process is repeated.

In table 1 are listed the selected values for the GA parameters used during the experiments.

Parameter	Value
Population size	50
Number of generations	30
Elitism count	2.5
Mutation probability	0.01
Crossover probability	0.8
Selection options	Roulette selection

Table 1: The parameters used in the GA.

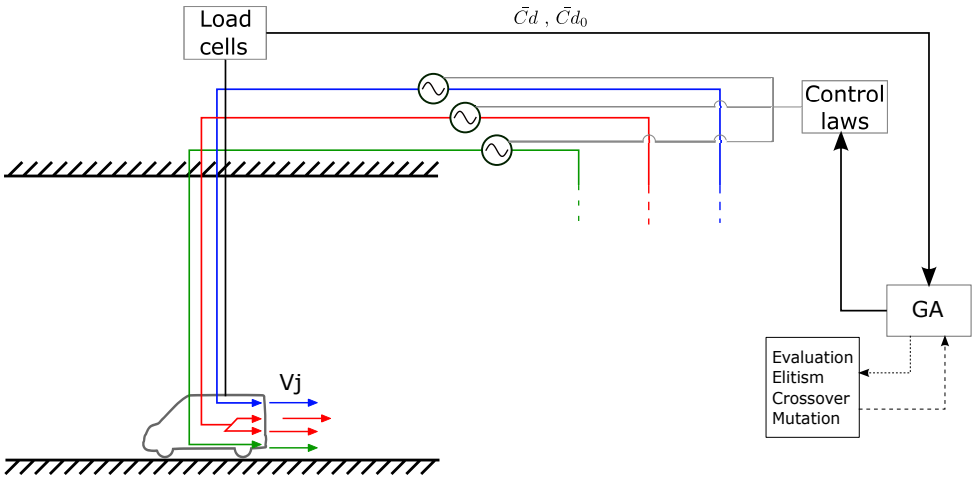

Figure 3: Schematic representation of the GA and its interaction with the experimental setup.

3.1. Implementation methodology

Figure 3 shows the interface between the GA and the experimental setup. The selected control law of the solenoid valves is the sum of two sine waves (figure 4), defined as:

$$V(t)=\left[\frac{V_{1,max}-V_{1,min}}{2}sin(2\pi f_1 t)+\frac{V_{1,max}+V_{1,min}}{2}\right]+\left[\frac{V_{2,max}-V_{2,min}}{2}sin(2\pi f_2 t)+\frac{V_{2,max}+V_{2,min}}{2}\right] \quad (2)$$

One single control law is defined for all the valves, to reduce the time needed to reach convergence for the GA. Future developments will also include the possibility of independently actuating the three valves, with the drawback of longer convergence times associated with a richer population size. This will allow the definition of the optimal forcing condition, accounting for the exploration of the entire parametric space.

The parameters to be optimised are six: two frequency values (f_1, f_2), two maximum ($V_{1,max}$, $V_{2,max}$) and two minimum voltage values ($V_{1,min}$, $V_{2,min}$).

The optimization is also constrained to take into account the operative conditions envelope of the solenoid valves. This yields the following constrains:

- $\left(\sum_{k=1}^{2} V_{max,k}\right) \leq 9.5\ V$

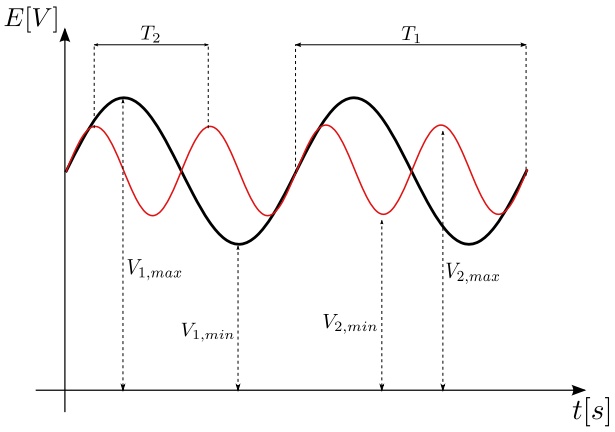

Figure 4: Schematic representation of the control law implemented in this work.

- $\left(\sum_{k=1}^{2} V_{min,k}\right) \geq 5.5\ V$
- $V_{max,i} > V_{min,i}$

where k indicates the number of waves included in the control law, while i indicates the i-th jet.

4. Results

4.1. Training

Figure 5 shows the convergence history of the percentage drag variation ($\Delta Cd\ \% = \frac{\overline{Cd}_0 - \overline{Cd}}{\overline{Cd}_0} \cdot 100$) as a function of the generations. This value closely resembles the behaviour of the fitness function (equation 1) maximised by the algorithm. In particular, the dashed black line, blue line and red line are representative of the mean, maximum and minimum value of $\Delta Cd\ \%$ across the entire population for each generation.

The data show that the algorithm tends towards a maximum value of the drag reduction that is 11.2%, within 30 generations, corresponding to a physical time of about 25 hours. Furthermore, the initial generations evidence the existence of control laws that are also detrimental from the drag reduction point of view, since the initial population is selected randomly. The algorithm quickly discards these options, retaining only those that are effective from the drag reduction point of view.

The exploration of the parametric space performed by the algorithm can be evidenced by the variation of the six parameters as a function of the generations. Figure 6 shows the maximum (blue dashed line), minimum (red dashed line), and fitness value (black dashed line) of the six parameters across the population, as a function of the generations. The fitness value represents the value of the parameter yielding the maximum of the fitness function.

A perfectly converged solution would be the case where maximum, minimum and fitness value are overlapping. Figure 6 show that the six parameters of the control law are all converging quite nicely. It is important to point out that the fairly quick convergence of the control parameters towards the fitness value does not hinder the exploration of the algorithm. It can be seen how initially a broad range of solutions are attempted by the system. Discarding those that are not effective from the drag reduction point of view allows to narrow down the parametric space towards the fitness value.

The convergence conditions reached by the GA are reported in table 2, with the corresponding value of the maximum percentage drag reduction. The values of $V_{max,i}$ and $V_{min,i}$ are condensed

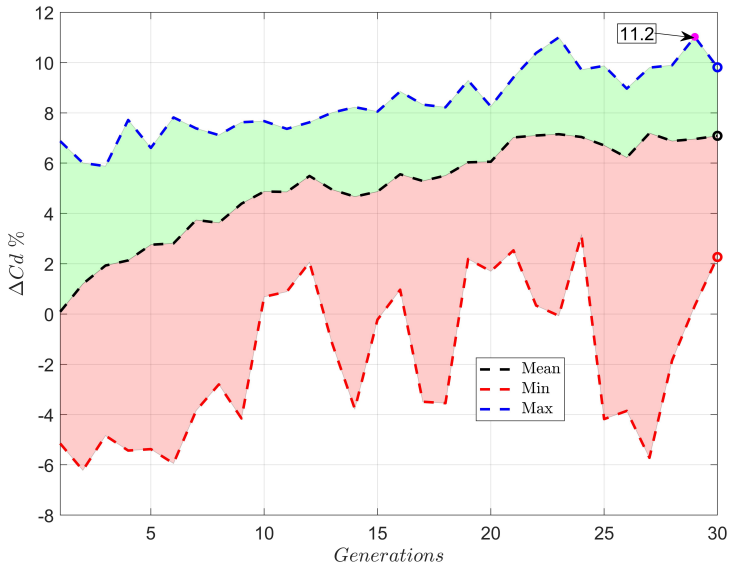

Figure 5: Percentage drag reduction ($\Delta Cd\%$) as a function of the generations. The label indicates the condition where the configuration yielding the maximum value of the drag reduction. Data are collected at $Re = 0.9 \cdot 10^5$. The number of elements in the population is equal to 50.

in the momentum coefficient, defined as

$$C\mu_i = \frac{V_{j,i}^2 S_{j,i}}{U_\infty^2 S} \tag{3}$$

where $V_{j,i}$ indicates the exit speed of the i-th jet, $S_{j,i}$ is the exit cross sectional area of the i-th jet, U_∞ is the freestream speed and $S = H\ W$ is a reference surface, taken as the cross section of the vehicle. The conversion between the actuation voltage and the jet exit speed ($V_{j,i}$) was obtained through a dedicated mapping function.

Parameter	Value
$C\mu_{top}$	0.0299
$C\mu_{bottom}$	0.0256
$C\mu_{lateral}$	0.0251
f_1/f_{max}	0.396
f_2/f_{max}	0.249
$\Delta Cd_{max}\%$	11.2

Table 2: Convergence parameters.

4.2. Base pressure analysis

The convergence conditions identified in table 2 were imposed to examine the resulting flow field and compare it with the natural condition. Figure 7 shows the distribution of the pressure

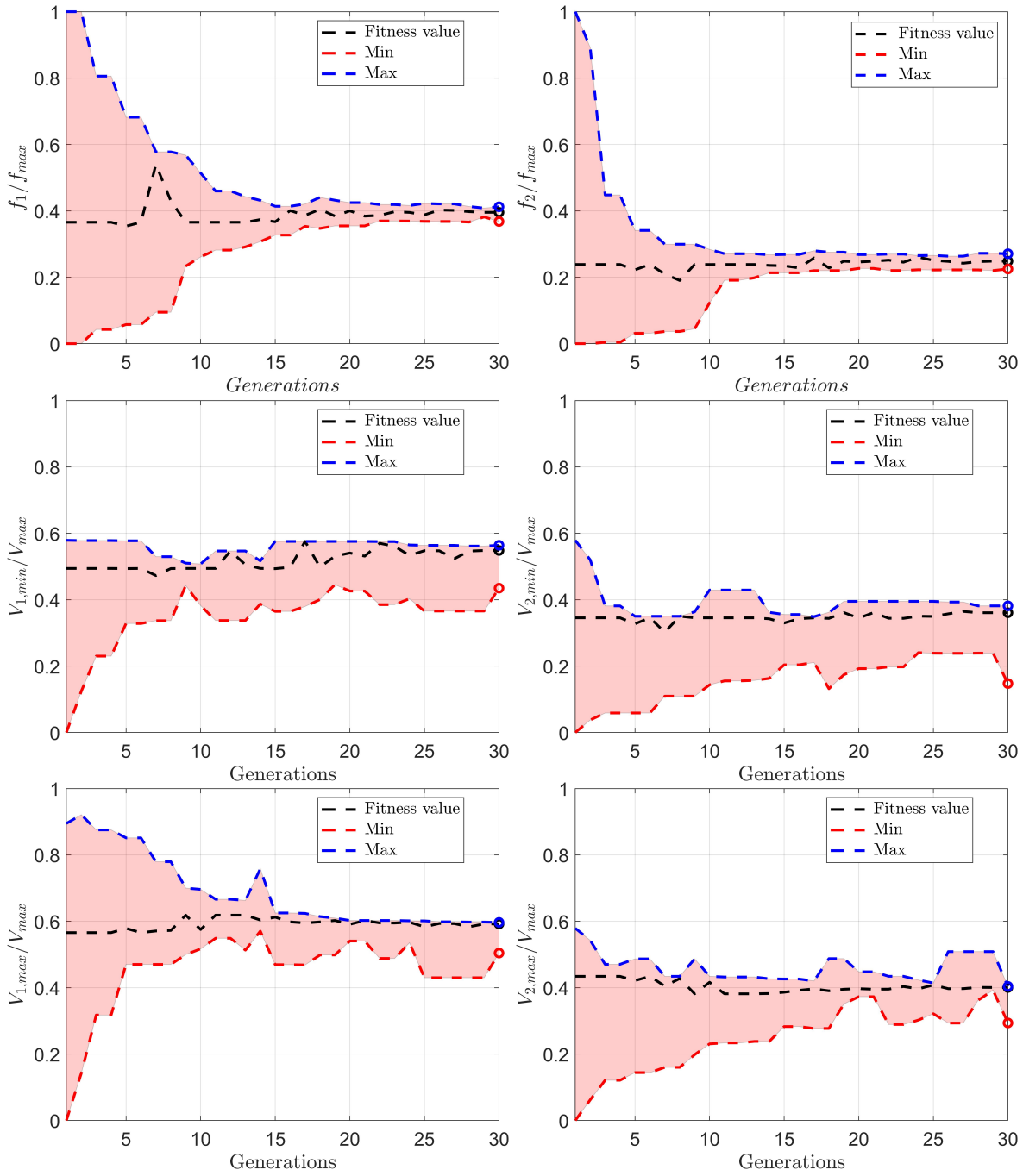

Figure 6: Forcing parameters for the pulsed actuation as a function of the generations at $Re = 0.9 \cdot 10^5$. On the left (right) column are reported the parameters for the first (second) sine wave. Elements in the population equal to 50.

coefficient $Cp = (p - p_\infty)/(0.5\rho U_\infty^2)$ in the natural (left-hand side) and the forced conditions (right-hand side).

The locations where the pressure is measured are highlighted with red circles. It must be noted that for the sake of comparison the data are mirrored about the XZ plane and reported on the same figure. These values are linearly interpolated to obtain the colormaps of figure 7.

The natural condition exhibits a large separated flow, with a downward pressure gradient as typical for bluff bodies with $H/W > 1$ ([3]). The mean value of the base pressure, limited to the investigated region, is $Cp_{mean,0} = -0.148$. The strong pressure imbalance between the front and the base of the vehicle is generally indicated as the main responsible for the high drag of bluff bodies. The corresponding value of the drag coefficient is $Cd_0 = 0.342 \pm 4.16E-3$ with a 95% confidence interval.

In the forced conditions the actuation significantly affects the pressure distribution across the base. A first, immediate consideration is that the actuation leads to a reversed sign of the pressure gradient, that is directed upwards. The mean value of the base pressure increases, attaining a value of $Cp_{mean} = 0.015$, thus confirming a strong pressure recovery. The corresponding value of the drag coefficient is $Cd = 0.304 \pm 3.70E-3$ with a 95% confidence interval.

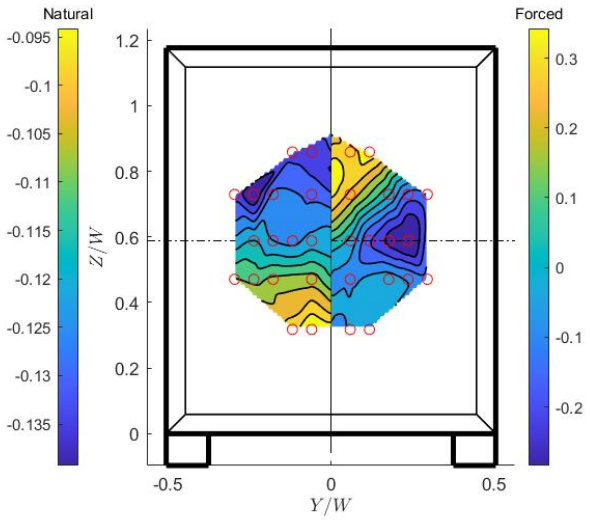

Figure 7: Colormaps of the pressure coefficient across the base: on the left (right) hand side the natural (forced) condition. To improve readability, two different ranges are used for the colormaps.

4.3. POD Analysis

The effect of the forcing condition on the wake dynamics is explored analysing the fluctuating pressure signals measured with the microphone capsules that are located across the base. In particular, the fluctuating pressure signals are used to perform a Proper Orthogonal Decomposition (POD). The aim of the POD analysis is to determine the most energy carrying modes, to evaluate the effect of the forcing on the structure of the wake. The POD technique decomposes the time signal into modes and coefficients [39].

Given a generic temporal signal $p'(Y, Z, t)$ this is decomposed into a sum of k modes each of which consists of a temporal coefficient $a_k(t)$ and an eigenfunction $\varphi_k(Y, Z)$ according to the following:

$$p'(y,z,t) = \sum_k a_k(t)\varphi_k(Y,Z) \tag{4}$$

where k indicates the number of modes. Each eigenfunction $\varphi_k(Y,Z)$ must satisfy the condition:

$$\int \left\langle p'(Y,Z,t) \cdot p'(Y,Z,t)^T \right\rangle_t \cdot \varphi_j(Y,Z) dydz = \lambda_j \cdot \varphi_j(Y,Z) \tag{5}$$

where j varies from 1 to the total number of probes, in this case the 12 microphone capsules and $\langle \cdot \rangle_t$ indicates the time average operation.

Figure 8 shows the energy distribution across the first twelve modes for the natural and forced cases. A stark difference can be immediately detected: while the unforced case features a first mode that carries about 80% of the total energy, in the forced case the energy is reduced to about 20%. The second mode, instead, evidences a switch of the energy content between the the natural and forced case. In fact, to the natural case is associated a much lower energy content (nearly 5%), while the forced case features energy values similar to the mode 1.

As evidenced in figure 9, the first two modes are mostly characterized by a shedding phenomenon. The first mode, in the natural case, shows traces of a three dimensional shedding occurring from the lateral, top and bottom edges of the base, with a prevalence of the shedding occurring with respect to the XY plane. On the other hand, figure 9 shows that the first mode in the forced condition is associated with a top-bottom shedding.

In the natural case, the second mode can be ascribed to the shedding occurring on the lateral edges of the base. A clear difference is instead detected in the forced case, which finds an anti-symmetric configuration with respect to mode 1.

The higher order modes contribute much less to the overall energy content and they feature a similar behaviour to the one of mode 2.

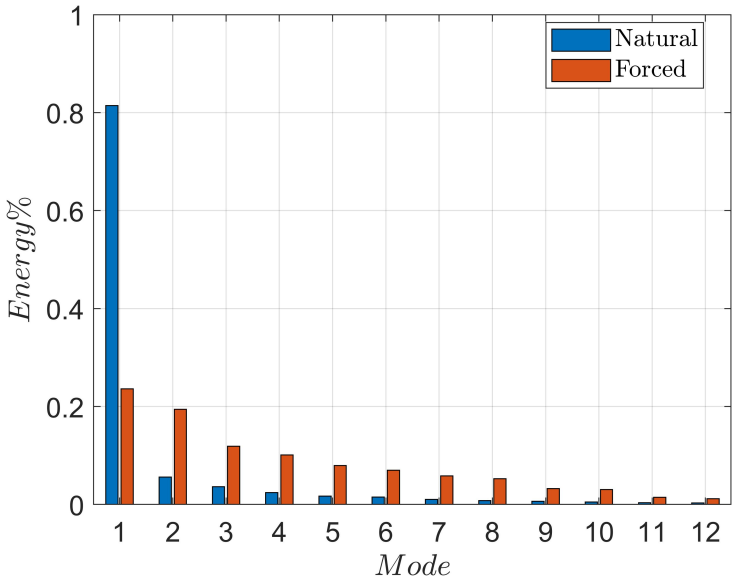

Figure 8: Energy distribution across the first twelve modes for the natural and forced condition.

5. Conclusions

In this work we demonstrated the possibility of applying a genetic algorithm based approach to control the near wake of a commercial road vehicle by means of pulsed air jets located along

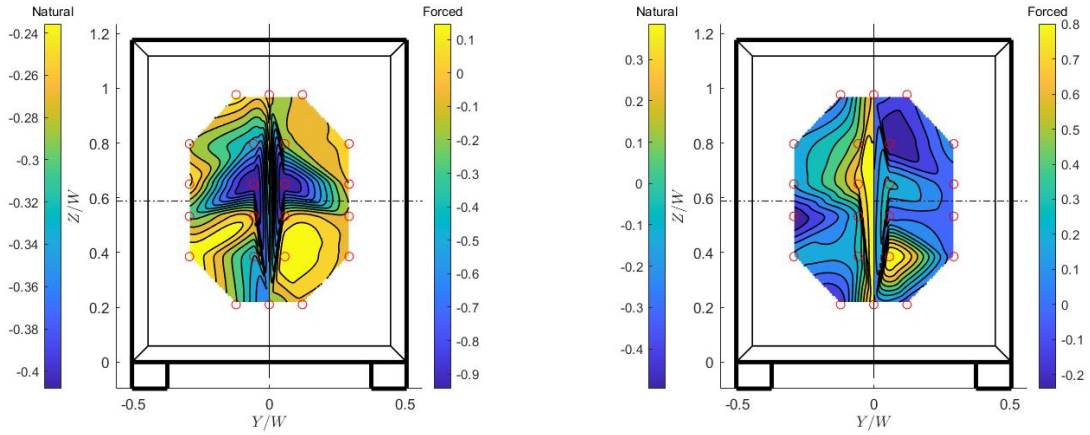

(a) (b)

Figure 9: Colormap of the fluctuating pressure signal for the first (a) and second (b) POD mode.

the model's base. The closed-loop control system is indeed capable of achieving drag reduction values as large as 11.2%.

The selected control law is the sum of two sine waves. The algorithm optimizes the values of the frequency and the amplitude of each of the two sine waves.

The system is capable of determining an optimal control law that minimizes a cost function, which is defined on the basis of the drag reduction with respect to the natural condition. The physical time needed to achieve a converged solution is approximately 25 hours.

The manipulated flow is investigated through the static pressure and microphone probes that populate the model's base.

The spatial distribution of the pressure coefficient reveals that the forcing leads to a switch of the direction of the pressure gradient across the base. Furthermore, a strong pressure recovery is experienced.

The POD analysis applied to the microphone probes reveals the following aspects: (i) the natural case has one dominant mode, that is representative of a three dimensional shedding, which should also includes a signature of the pumping phenomenon, although not clearly evidenced by the present investigation; (ii) the first mode for the forced case is instead mainly associated with a top-down shedding (i.e. with respect to the XY), and finds a symmetric configuration in the mode 2.

References

[1] Gilliéron P and Kourta A 2009 *Experiments in Fluids* **48** 1–16
[2] Schoettle B, Sivak M and Tunnell M 2016 *American Transportation Research Institute*
[3] Grandemange M, Gohlke M and Cadot O 2013 *Journal of Fluid Mechanics* **722**
[4] Cerutti J J, Sardu C, Cafiero G and Iuso G 2020 *Fluids*
[5] Cerutti J J, Cafiero G and Iuso G 2021 *International Journal of Heat and Fluid Flow* **90**
[6] Grandemange M, Gohlke M and Cadot O 2013 *Physics of Fluids* **725**
[7] Rigas G, Oxlade A, Morgans A and Morrison J F 2014 *Journal of Fluid Mechanics* **755**
[8] Evstafyeva O, Morgans A and Longa L 2017 *Journal of Fluid Mechanics* **917**
[9] Haffner Y, Borée J, Spohn A and Castelain T 2020 *Journal of Fluid Mechanics* **894**

[10] Iuso G 1985 *18th Fluid Dynamics and Plasmadynamics and Lasers Conference*

[11] Walsh M J and Anders J B 1989 *Applied Scientific Research 1989 46:3* **46**(3) 255–262 ISSN 1573-1987

[12] Iuso G and Onorato M 1995 *Meccanica* **30**(4) 359–376 ISSN 1572-9648

[13] Beaudoin J F and Aider J L 2008 *Experiments in Fluids* **44** 491–501

[14] Pujals G, Depardon S and Cossu C 2010 *Experiments in Fluids* **49** 1085–1094

[15] Kim D, Lee H, Yi W and Choi H 2016 *Bioinspiration & Biomimetics* **11** 026004

[16] Capone A and Romano G 2019 *Journal of Wind Engineering & Industrial Aerodynamics* **185**

[17] Cafiero G, Castrillo G, Greco C S and Astarita T 2019 *Experimental Thermal and Fluid Science* **102** 302–315 ISSN 08941777

[18] Gehlert P, Cherfane Z, Cafiero G and Vassilicos J C 2021 *AIAA Journal* **59**(5) ISSN 1533385X

[19] Iuso G, Onorato M, Spazzini P G and Di Cicca G M 2002 *Journal of Fluid Mechanics* 23–58 ISSN 00221120

[20] Choi H, Jeon W P and Kim J 2008 *Annual Review of Fluid Mechanics* **40** 113–139

[21] Longa L D, Morgans A S and Dahan J A 2017 *Theoretical and Computational Fluid Dynamics* **31** 567–577

[22] Li R, Barros D, Borée J, Cadot O, Noack B and Cordier L 2016 *Experiments in Fluids* **57** ISSN 0723-4864 publisher Copyright: © 2016, Springer-Verlag Berlin Heidelberg. Copyright: Copyright 2017 Elsevier B.V., All rights reserved.

[23] Cannata M, Cafiero G and Iuso G 2020 *AIAA Journal* **58** 2042–2052 ISSN 00011452

[24] Minelli G, Dong T, Noack B R and Krajnović S 2020 *Journal of Fluid Mechanics* **893**

[25] Marusic I, Chandran D, Rouhi A, Fu M K, Wine D, Holloway B, Chung D and Smits A J 2021 *Nature Communications 2021 12:1* **12**(1) 1–8 ISSN 2041-1723

[26] Barros D, Borée J, Noack B R, Spohn A and Ruiz T 2016 *Journal of Fluid Mechanics* **805**

[27] Barros D, Borée J, Noack B R and Spohn A 2016 *Physics of Fluids*

[28] Lasagna D, Orazi M and Iuso G 2013 *Physics of Fluids* **25**(1) 017101 ISSN 1070-6631

[29] Lasagna D, Fronges L, Orazi M and Iuso G 2015 *AIAA Journal* **53**(10) 2920–2935 ISSN 00011452

[30] Gautier N, Aider J L, Duriez T, Noack B R, Segond M and Abel M 2015 *Journal of Fluid Mechanics* **770** 442–457 ISSN 0022-1120

[31] Duriez T, Brunton S L and Noack B R 2017 *Machine Learning Control (MLC)* vol 116 (Springer, Cham)

[32] Li R, Noack B R, Cordier L, Borée J and Harambat F 2017 *Experiments in Fluids* **58**(8) 1–20 ISSN 07234864

[33] Fan D, Yang L, Wang Z, Triantafyllou M S and Karniadakis G E 2020 *Proceedings of the National Academy of Sciences of the United States of America* **117** 26091–26098 ISSN 10916490

[34] Wang J, Minelli G, Cafiero G, Iuso G, He K, Basara B, Gao G and Krajnovic S 2022 *under review from Journal of Fluid Mechanics*

[35] Castelain T, Michard M, Szmigiel M, Chacaton D and Juvé D 2018 *Journal of Wind Engineering and Industrial Aerodynamics* **175** 352–363 ISSN 01676105

[36] Sardu C, Lasagna D and Iuso G 2016 *Journal of Fluids Engineering*

[37] Goldberg D E 1989 *Genetic Algorithms in Search, Optimization and Machine Learning* 1st ed (USA: Addison-Wesley Longman Publishing Co., Inc.) ISBN 0201157675

[38] Conn A R, Gould N I M and Toint P 1991 *SIAM Journal on Numerical Analysis* **28** 545–572

[39] Berkooz G, Holmes P and Lumley J L 1993 *Annual Review of Fluid Mechanics* **25** 539–575